Kovove Mater. 60 2022 209–222
DOI: 10.31577/km.2022.4.209

Metallurgical characterization of natural aging effects on pre-deformed Al 7075/T651 alloy during retrogression and re-aging heat treatment

Gözde Altuntaş*, Bülent Bostan

Gazi University, Faculty of Technology, Department of Metallurgical and Materials Engineering, Ankara, Turkey

Received 20 January 2022, received in revised form 18 April 2022, accepted 12 May 2022

Abstract

In this study, a new heat treatment route was designed, and the effects of pre-deformation on the retrogression and re-aging (RRA) and 17500 h natural aging (NA) heat treatment were investigated. The specimens that were pre-deformed during the RRA heat treatment and the subsequent NA specimens were compared. As a result of the heat treatments, the phase volume ratios in each specimen were calculated and compared with two different methods. Firstly, the distributions of the phases and the geometrical changes of the precipitates were interpreted by scanning electron microscopy (SEM). Elemental ratios in the precipitates were obtained by energy-dispersive X-ray spectrometry (EDS). Particle size, dislocation density, lattice strain, and texture coefficient values were calculated by the X-ray diffraction method (XRD), and their effects on crystallography were examined in detail. As a result of the differential scanning calorimetry (DSC) analysis, it was observed that the transformation temperatures of the phases changed with the heat treatment route. As a result of all analyses, the connections between the hardness values were interpreted. The results showed that the hardness values, dislocation densities, and lattice strain of the pre-deformed RRA + NA specimens were increased compared to the pre-deformed RRA specimens.

Key words: natural aging, retrogression and re-aging heat treatment, dislocation density, texture coefficient, 7075 aluminum alloys

1. Introduction

7000 series (Al-Zn-Mg-Cu) aluminum alloys have high hardness and strength and can be hardened by precipitation [1, 2]. Due to their low densities, they have been frequently used in the defense industry, space, and aviation in recent years and can compete with steel at the same time [3]. The aging process of these alloys generally continues with natural aging after solution heat treatment followed by quenching. However, the long duration of natural aging makes artificial aging heat treatment more frequently used. Natural aging has a more profound effect on microstructural properties than artificial aging. Therefore, it is necessary to fully understand the precipitates during natural aging [4–6]. The order of precipitation in 7000 series alloys was accepted as follows [7, 8]:

Solid solution/GP zones/metastable η'/stable η-$MgZn_2$.

There are two types of GP zones. GPI zones are created over a wide temperature range from room temperature to 140–150 °C. It is often seen when natural aging is done. It is consistent with the internal ordering of Zn and Al/Mg on the matrix lattice. GP II zones are formed by aging at temperatures above 70 °C after quenching at temperatures above 450 °C [9]. Some studies suggest that the GPI zones formed during aging at a low temperature dissolve at 120 °C and form GP II zones that can transform to η' to gain strength [10]. Others suggest that the GPI zones are the core of the η' phase [11, 12]. It is thought that the metastable η' phase is the main strengthening phase and provides the hardening of the aged 7000 series alloys [13]. The η phase consists of $MgZn_2$ precipitates, which tend

---

*Corresponding author: e-mail address: gozdealtuntas@gazi.edu.tr to disperse at grain boundaries obtained at temperatures up to 350 ℃. It is non-congruent and usually nucleates at a non-congruent or semi-congruent interface. It creates non-congruent boundaries with the Al matrix [14, 15]. Different heat treatments applied to Al-Zn-Mg-Cu alloy establish a relationship between strength and corrosion resistance. Maximum strength value is obtained by applying T6 heat treatment, while strength is reduced by applying T7X heat treatment, and corrosion resistance is improved [16, 17]. Retrogression and re-aging (RRA) heat treatment was applied to increase strength and corrosion resistance simultaneously. The RRA heat treatment was developed by Cina and Gan, who worked in an Israeli aircraft company in 1974 with a patent [18, 19]. The Precipitate Free Zone (PFZ) is found around the lower grain boundaries and dispersoids in aging alloys, primarily the grain boundary. The formation of the precipitate-free zone occurs during the rapid cooling after quenching by the coalescence of atomic cavities at the high-energy grain boundaries, reducing the zones where the precipitates will nucleate and the number of solute atoms. 7000 series Al alloys have a PFZ. The disappearance of the atomic spaces formed around the grain boundary is an important factor in the formation of PFZ. This zone plays an effective role in the mechanical and corrosion properties of Al-Zn-Mg-Cu alloys. As a result of the aging heat treatment applied at 120–180 ℃, it has been observed that the increasing aging temperature creates a wider PFZ area [20, 21].

Recent research using advanced atomic imaging has found that GP II zones have $\mathrm{GP}_{\eta'}$ and $\mathrm{GP}_{\eta\mathrm{p}}$ zones, depending on the alloy composition. In an alloy with a Zn/Mg ratio > 2, $\mathrm{GP}_{\eta\mathrm{p}}$ zones are formed. The $\mathrm{GP}_{\eta\mathrm{p}}$ zones are distinguished by their characteristic thickness of 7 atomic layers and structurally stable diatomic panels, and they transform to η'_{p} instead of η'. It has been suggested that $\mathrm{GP}_{\eta\mathrm{p}}$ zones are dynamic precipitates during thermal aging; that is, each $\mathrm{GP}_{\eta\mathrm{p}}$ zone is formed differently from the other. In alloys with a Zn/Mg ratio < 2, $\mathrm{GP}_{\eta'}$ zones are formed. The $\mathrm{GP}_{\eta'}$ zones do not have a significant thickness, which they have on {111}Al [22–23].

J. Liu et al. [24] observed $\mathrm{GP}_{\eta'}$ (GP II) zones in naturally aged specimens for the first time. They exhibit very slow formation kinetics with a Zn/Mg ratio of approximately 1.3–1.4. It was found that $\mathrm{GP}_{\eta'}$ zones formed more slowly at room temperature and provided stronger hardening effects than early clusters. Therefore, it was thought that they could act as the core of η'-phase formation during subsequent artificial aging.

S. Liu et al. [25] found that after a long period of natural aging, the rapidly cooled specimens had a higher volume fraction of GP zones and, therefore, a higher increase in hardness than the slowly cooled specimen. During short aging times, small GPI zones are rich in Mg with a Zn/Mg ratio of about 0.9, but larger GPI zones have a higher Zn/Mg ratio, consistent with an equilibrium value [26].

Table 1. Chemical composition of Al 7075/T651 alloy (wt.%)

Elements (wt.%)								
Fe	Si	Mn	Cr	Ti	Cu	Mg	Zn	Al
0.5	0.4	0.3	0.28	0.2	2	2.9	6.1	Balance

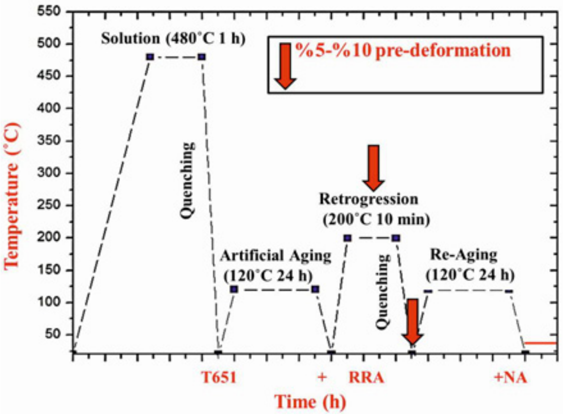

Fig. 1. Heat treatment cycle applied to Al 7075 T651 alloy.

The precipitation kinetics of GP zones, metastable η', and stable η phases in Al-Zn-Mg alloys were investigated. Accordingly, the apparent activation energies for GP, η' and η phases with the DSC technique were first determined by using JMAK isothermal calculation method and calculated as 56, 79, and 96 kJ mol^{-1} and calculated by the non-isothermal Kissinger calculation method as 57, 82, and 99 kJ mol^{-1}, respectively [27].

This study investigated the effects of long-term natural aging on the pre-deformed Al-Zn-Mg-Cu alloy during RRA heat treatment by creating a new heat treatment route. Transformations of GP zone, η' and η phases were observed by this heat treatment method. Furthermore, its effects on crystallography have been studied in detail with some calculations. As a result of the studies, 7000 series of Al alloys used in the aviation industry will be significantly affected by the increase in strength.

2. Experimental procedure

In the experimental study, commercially available 7075 aluminum sheet material with T651 heat treat-

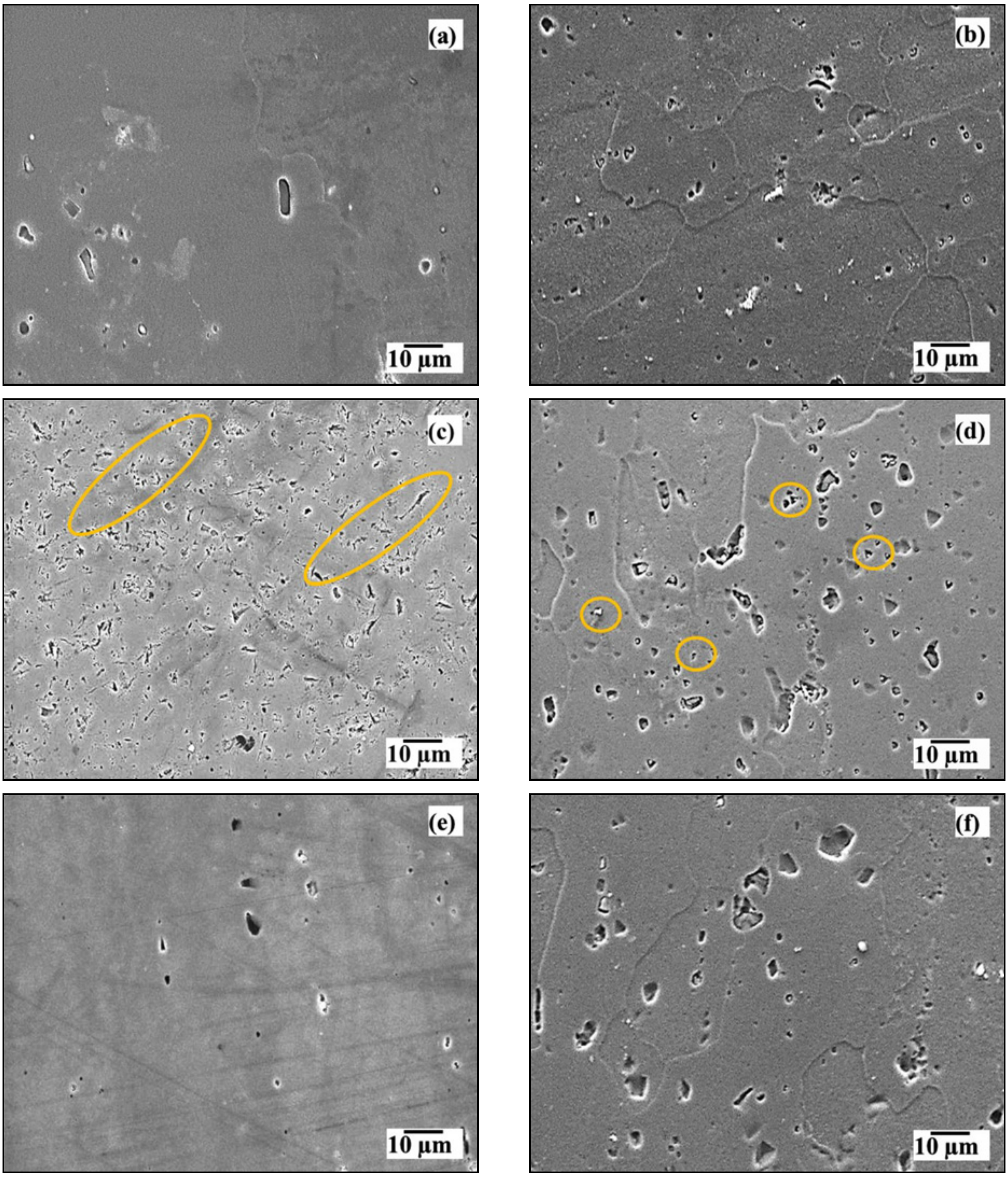

Fig. 2a–f. SEM microstructure images of (a) S specimen, (b) S + NA specimen, (c) 5Q specimen, (d) 5Q + NA specimen, (e) 10Q specimen, (f) 10Q + NA specimen.

ment was used. This material is coded as S. The chemical composition of the material in % by weight is given in Table 1.

The heat treatment cycle applied to the Al 7075/T651 alloy is given in Fig. 1. First, the RRA heat treatment was carried out in an SFL (SC 1206 model) brand chamber type horizontal high-temperature furnace under an argon atmosphere. Pre-deformation processes were carried out on an Instron 3369 computer-controlled universal testing machine with a tensile-compression capacity of 50 kN (5 t). Accordingly, resolution (retrogression) and 5–10 % pre-deformation were applied by keeping it at 200 ℃ for 10 min. It was then quenched and artificially aged at 120 ℃ for 24 h. These specimens were coded as 5Q and 10Q. Other specimens were kept at 200 ℃ for 10 min and quenched. Then 5–10 % pre-deformation was applied and re-aged at 120 ℃ for 24 h.

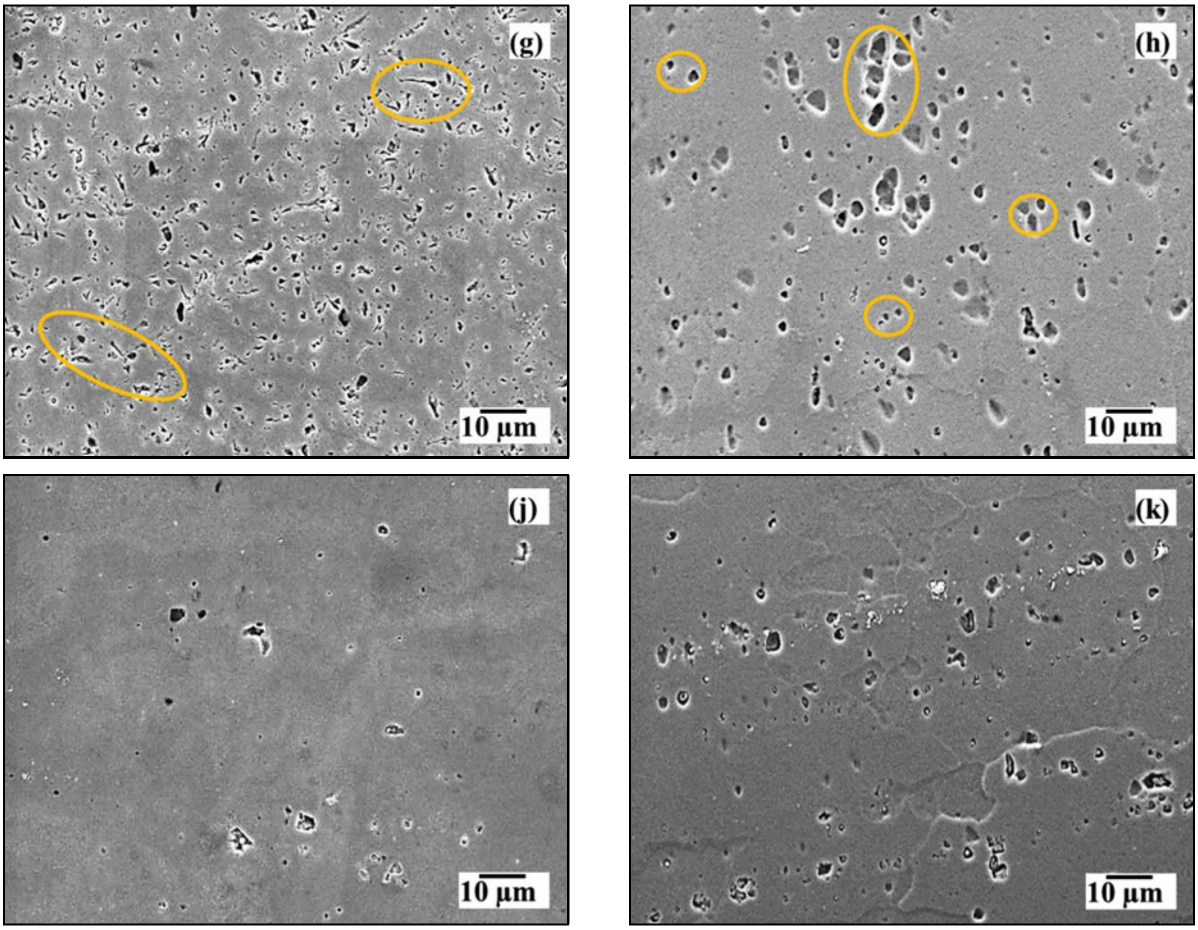

Fig. 2g–k. SEM microstructure images of (g) Q5 specimen, (h) Q5 + NA specimen, (j) Q10 specimen, and (k) Q10 + NA specimen.

These specimens were coded as Q5 and Q10. Finally, these specimens were naturally aged 17500 h at room temperature after RRA heat treatment. These specimens were coded as 5Q + NA, 10Q + NA, Q5 + NA, Q10 + NA. Microhardness tests of the specimens were determined by taking the hardness values from at least five points for each specimen in the Qness Hardness device, and the average HV0.5 values were determined. JEOL JSM-6060LV Scanning Electron Microscope (SEM) was used in microstructure studies. Elemental distributions were obtained with the JEOL JSM 6060LV Energy-Dispersive X-Ray Spectrometer (EDS, IXRF Sys.). Phase volume ratios of the specimens were calculated using Dewinter Material Plus 6.1 software on SEM microstructure pictures. At the same time, the results were compared using the point count method while calculating the phase volume ratio. XRD patterns were obtained using the Bruker D8 Advance XRD instrument. Monochromatic CuKα beam ($\lambda = 1.54056$ Å) was used as an X-ray source, and patterns were obtained at 40 kV and 40 mA. Specimens were scanned at a scanning speed of 0.04 in the range of 2θ 16°–80°. X-ray analysis calculated the particle size, dislocation density, lattice strain, and texture coefficient values of the specimens. HITACHI DSC 7020 thermal analysis unit was used to perform differential scanning calorimetry (DSC) experiments. The tests were carried out in an argon atmosphere with a heating rate of 10 ℃ min^{-1} and a temperature range of 25 to 460 ℃. It was tested with specimens of 10 mg mass enclosed in aluminum pans.

3. Results and discussion

3.1. Microstructure

As can be seen in Figs. 2a,b, when the natural aging process is added to the T651 heat treatment, the secondary phases increase. In Figs. 2c–g of the microstructure, it is thought that secondary phases before natural aging are seen in elongated form due to deformation. In Figs. 2d–h of the microstructure, 5 % of the energy resulting from deformation after natural aging is spent on secondary phase transformation, and secondary phase forms become spherical (yellow shapes shown on microstructure). Secondary phases in the microstructure in Figs. 2e–i increased in size with

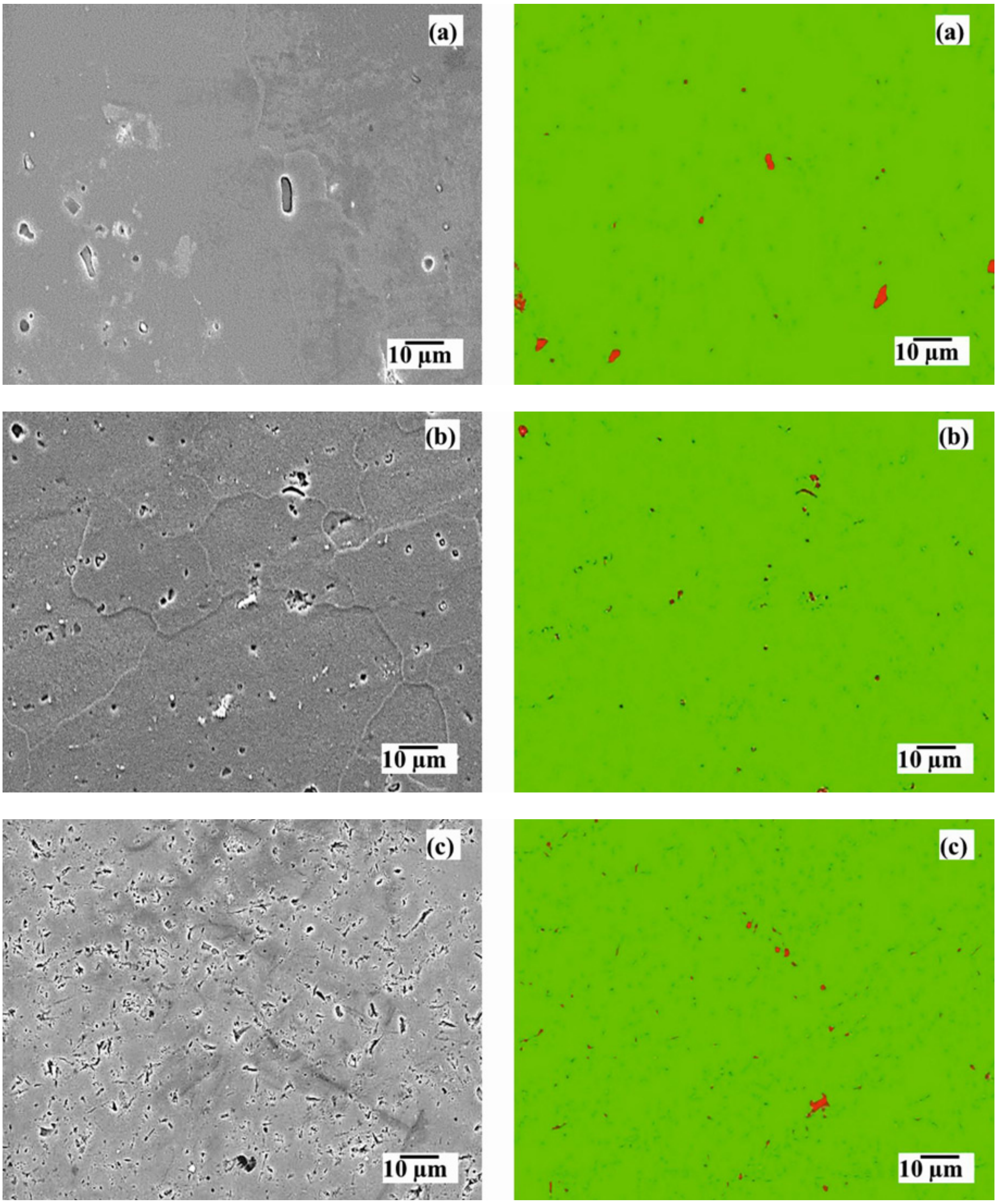

Fig. 3a–c. Distribution of the phase-volume ratios of the specimens (a) S, (b) S + NA, (c) 5QR.

natural aging, as in the microstructure in Figs. 2f–k. It was observed that the secondary phase distributions of the 10 % deformation applied samples were less than the 5 % deformation applied samples. This is because the driving force for the formation of potential nucleation sites in the matrix is 5 % pre-deformation. It is thought that the effect of this driving force is reduced by a 10 % pre-deformation rate. Experimental studies show that potential nucleation sites in the matrix do not increase with an increasing amount of pre-deformation [28].

Phase volume ratios of the specimens calculated using Dewinter Material Plus 6.1 software, respectively: (a) S 1.89 %, (b) S + NA 2.67 %, (c) 5QR 3.48 %, (d) 5QR + NA 5.68 %, (e) 10QR 0.78 %, (f) 10QR + NA 4.43 %, (g) Q5R 3.99 %, (h) Q5R + NA 4.52 %, (j) Q10R 1.83 %, and (k) Q10R + NA 5.61 %. It can be seen from Fig. 3 that the phase volume ratio in-

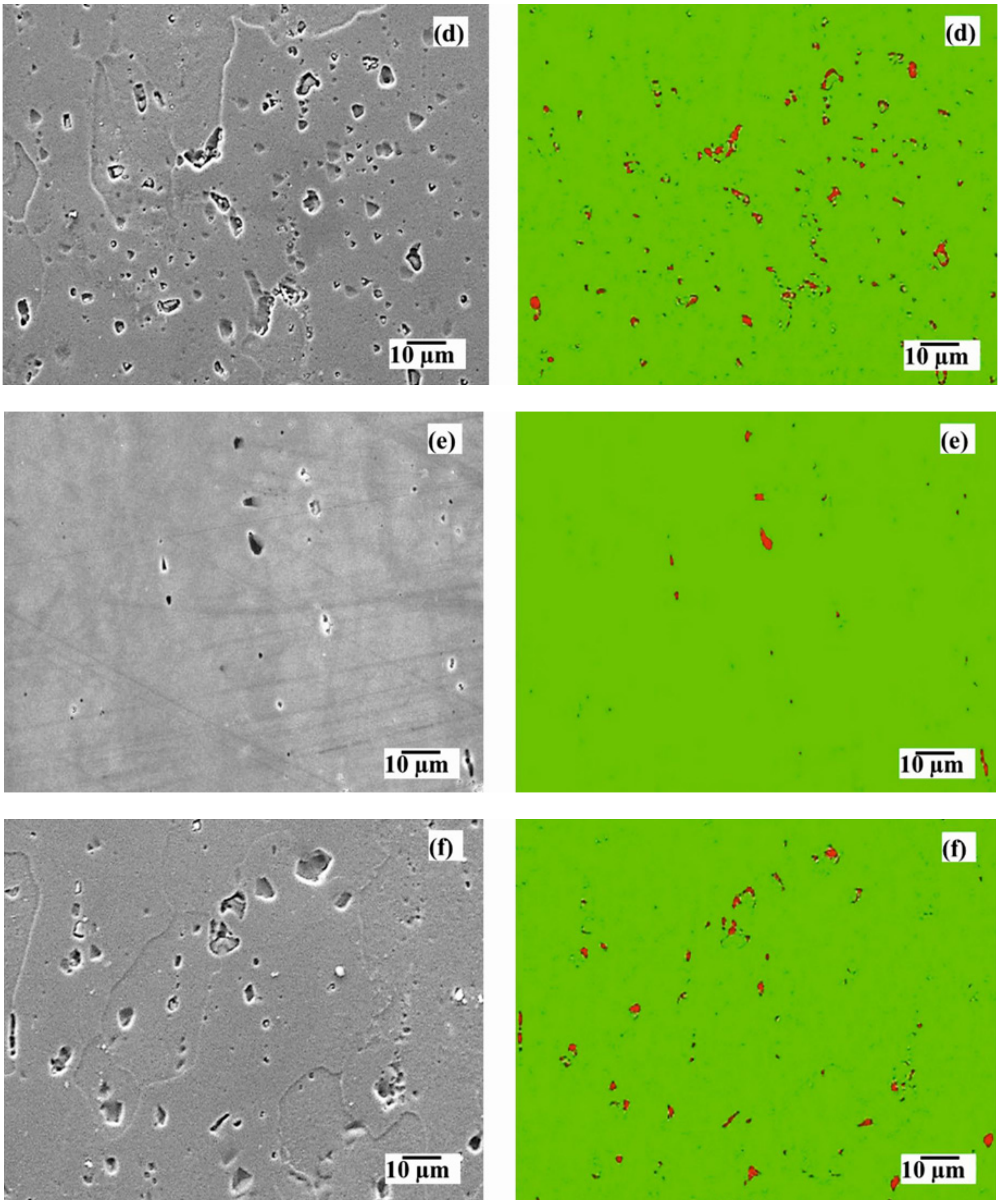

Fig. 3d–f. Distribution of the phase-volume ratios of the specimens (d) 5QR + NA, (e) 10QR, (f) 10QR + NA.

creased in all specimens with natural aging (17500 h) after RRA heat treatment.

In calculating the phase volume ratios, the point-counting method given by Eq. (1) was also used [29]. Phase volume ratio measurement was performed on the microstructure image of the Q5R + NA specimens taken at 500 × magnification. As a result of the calculation, it was found that it had a phase volume ratio of 5.71 %. Using Dewinter Material Plus 6.1 software, the result was 5.68 %. The approximate value of the results supports the calculation:

$$V_{\text{phase}} = P_{\text{phase}}/P_{\text{T}}, \qquad (1)$$

where V_{phase} is phase volume ratio ($V_{\text{phase}} = 4(1/2)/35 \times 100 = 5.71\,\%$), P_{phase} is number of points corresponding to the phase, and P_{T} is total number of points.

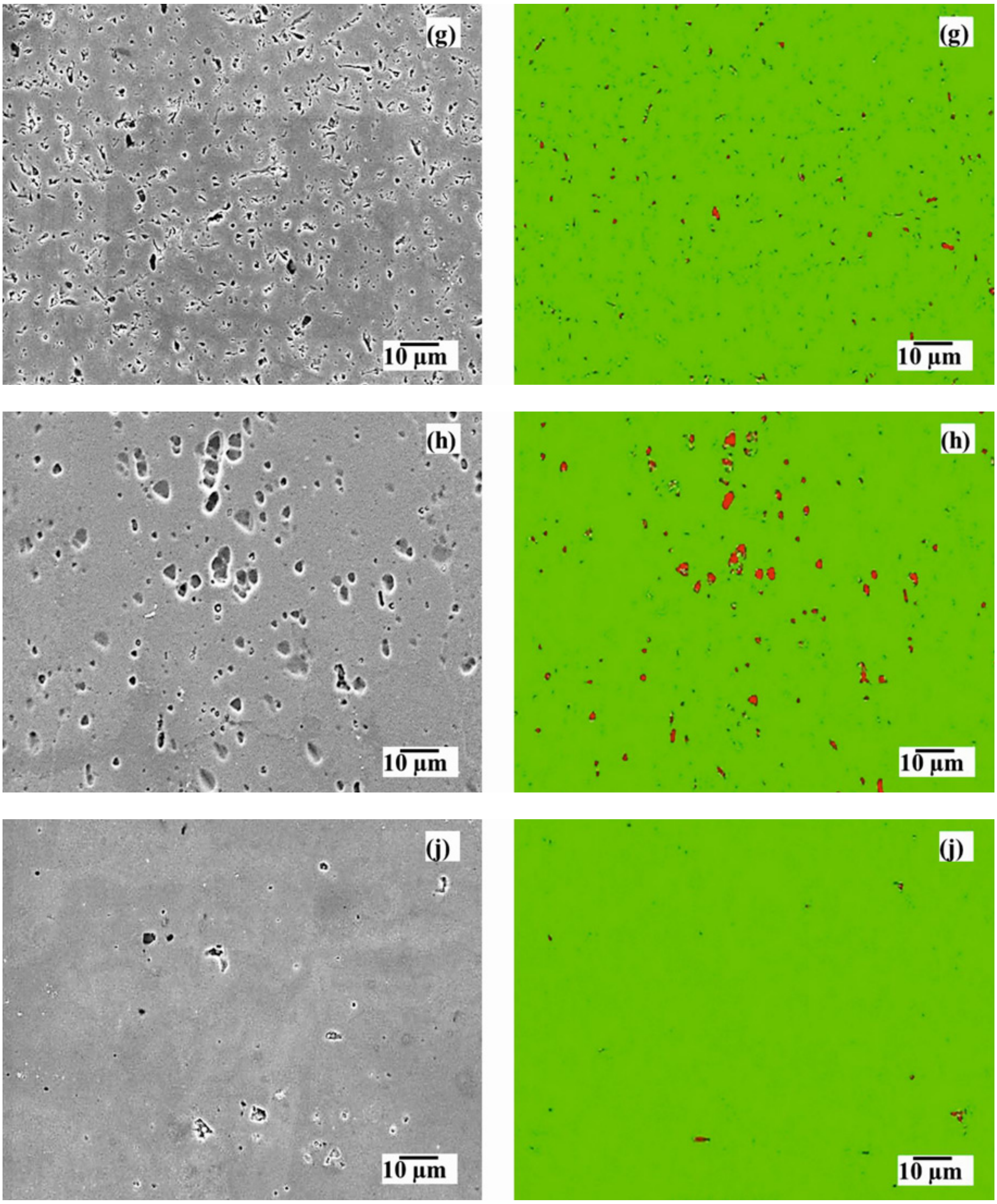

Fig. 3g–j. Distribution of the phase-volume ratios of the specimens (g) Q5R, (h) Q5R + NA, (j) Q10R.

Figure 4 shows the Mg/Zn ratios and dot-line EDS analyses of pre-deformed specimens during the RRA heat treatment and then naturally aged. EDS analyses were made from 10 different precipitates. In the EDS analysis of points 3, 7, and 9, the Zn/Mg < 2 ratio was found. These precipitates are smaller in size compared to the others. The lowest Zn ratio was observed in these small-sized precipitates. It is known that GP$_{\eta'}$(GP II) zone occurs in alloys with a Zn/Mg ratio < 2. Zn/Mg > 2 was found in 1, 2, 4, 5, 6, 8, and 10 point ESD analyses. These precipitates are GP$_{\eta\mathrm{p}}$ regions (GP II). GP$_{\eta\mathrm{p}}$ zones transform to η'_{p} instead of η'. It has been suggested that all GP$_{\eta\mathrm{p}}$ zones are formed differently from the others [22, 23]. According to the line EDS analysis on the precipitates, Al gives more homogeneous intensity along the whole line. On the other hand, it was observed that the Mg-Zn ratio was more intense in the regions with secondary phases

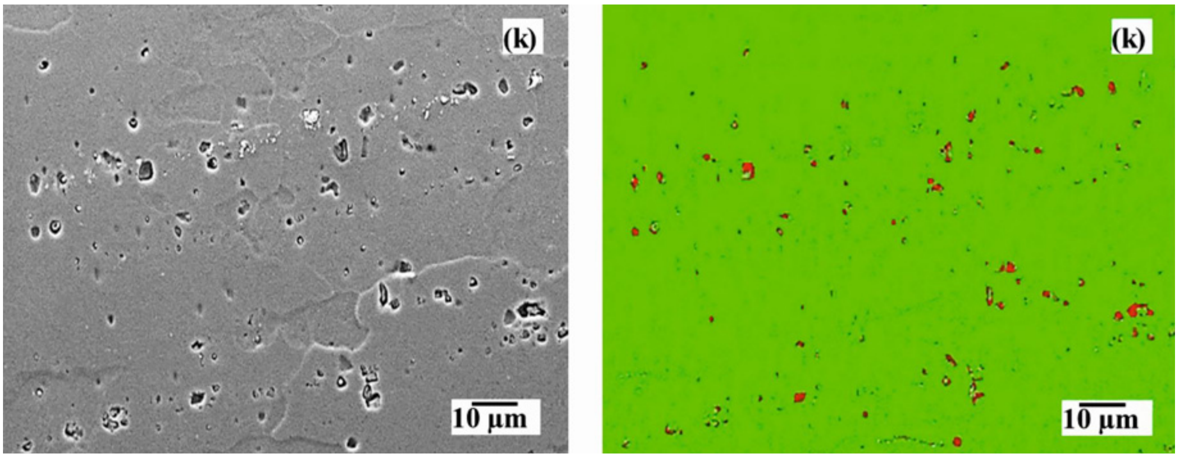

Fig. 3k. Distribution of the phase-volume ratios of the specimens (k) Q10R + NA.

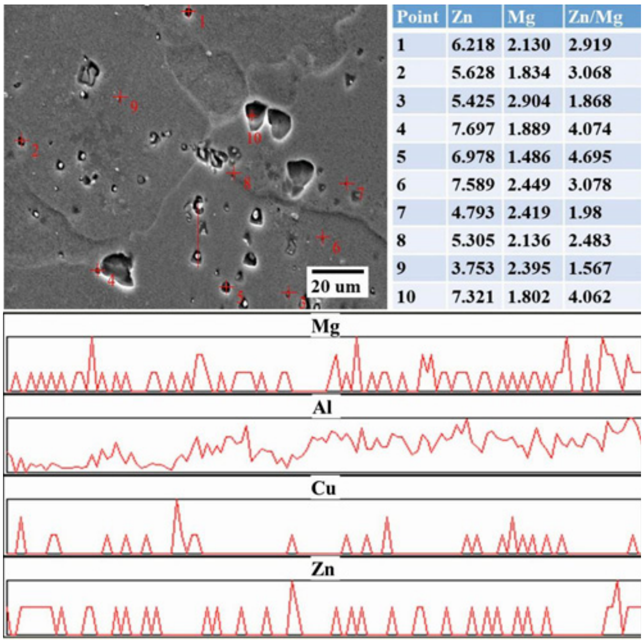

Point	Zn	Mg	Zn/Mg
1	6.218	2.130	2.919
2	5.628	1.834	3.068
3	5.425	2.904	1.868
4	7.697	1.889	4.074
5	6.978	1.486	4.695
6	7.589	2.449	3.078
7	4.793	2.419	1.98
8	5.305	2.136	2.483
9	3.753	2.395	1.567
10	7.321	1.802	4.062

Fig. 4. Mg/Zn ratios and EDS analyses of specimens in which the RRA + NA were applied.

due to the presence of $MgZn_2$.

Figure 5 shows the schematic representation of the precipitates and phases formed due to different heat treatments. Since there is artificial aging with T651 heat treatment, the GP II zone and η' phase are formed. When the RRA treatment is added to the T651 heat treatment, a small amount of GP I zone (smaller precipitates < 3 nm) and η phase also begin to appear in the structure. It has been reported that the GP I zone appears as clusters with enriched dissolved elements and has ultrafine dimensions in the first aging phase [30, 31]. When natural aging is added to the T651 + RRA heat treatment, it has been shown that the sizes of the η and η' phases increase, and their number increase as well.

3.2. Hardness properties

Figure 6 shows the microhardness results of specimens in which pre-deformation was applied at different rates. The hardness of the specimens in which T651 + RRA was applied was measured as 242 HV0.5 (5Q), 253 HV0.5 (Q5), 252 HV0.5 (10Q), and 264 HV0.5 (Q10), respectively. The hardnesses of the specimens in which T651 + RRA + NA was applied were measured as 247 HV0.5 (5Q + NA), 259 HV0.5 (Q5 + NA), 257 HV0.5 (10Q + NA), and 267 HV0.5 (Q10 + NA), respectively. T651 + RRA + 175000 h natural aging increased the hardness values in all specimens. The precipitates distributions and phase-volume ratios in the microstructures also support this situation. The increasing amount of pre-deformation increased the hardness of all specimens. In addition, specimens

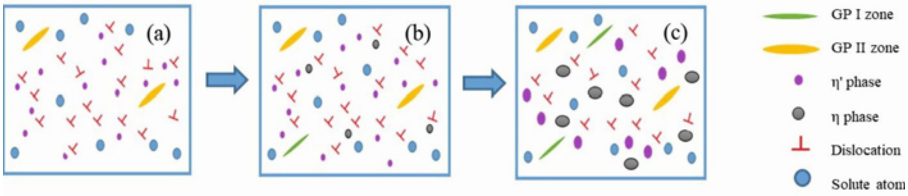

Fig. 5. Schematic representation of the precipitates and phases of the different heat-treated specimens: (a) 7075/T651, (b) 7075/T651 + RRA, and (c) 7075/T651 + RRA + NA.

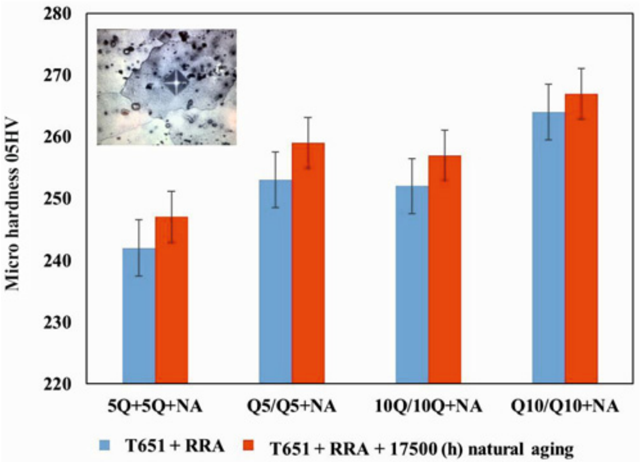

Fig. 6. Microhardness results of specimens subjected to pre-deformation at different rates.

deformed after retrogression at 200 °C (Q5R, Q5R + NA, Q10R, and Q10R + NA) were found to have higher hardness than those deformed during retrogression (5QR, 5QR + NA, 10QR, and 10QR + NA).

3.3. XRD studies

Figure 7 shows XRD analyses of specimens pre-deformed during RRA and specimens pre-deformed during RRA and then naturally aged. A standard reference pattern (JCPDS:01-089-4037) for aluminum was used to detect crystallographic planes. As a result of the XRD analysis, the intensity of the purchased S specimen was measured as the lowest. The (111) plane gave the most intense XRD peak. This plane shows the most intense XRD peak recommended for Al alloys [32]. However, the most intense XRD peak was observed in the (200) plane due to the RRA heat treatment and pre-deformation effect. In addition, the intensity at all peaks in the 5Q, 10Q, Q5, and Q10 specimens increased compared to the S specimens. With natural aging (S + NA) on the S specimen, the most intense peak intensity was seen in the (200) plane. It is understood from this that the natural aging heat treatment also changed the most intense peak plane proposed. It was observed that the peak intensities measured in S + NA, 5Q + NA, 10Q + NA, Q5 + NA, and Q10 + NA specimens were higher than those of S, 5Q, 10Q, Q5, and Q10 specimens.

Debye Scherrer's formula was used to measure the particle size and dislocation density of the specimens. FWHM (Full Width Half Maximum) value was also calculated from XRD peaks and applied in this formula. Particle size is also calculated using the Williamson–Hall equation. The well-known Williamson-Hall equation determined the lattice strain calculations of the specimens [33]. Debye Scherrer's formula [34], Eq. (2):

$$D_\mathrm{p} = k\lambda/\beta\cos\theta, \tag{2}$$

where D_p is crystallite size (m), k is constant; $k = 0.94$ (for cubic structures), λ is the wavelength of X-ray used (1.54×10^{-10} m), β is FWHM of a diffraction peak (radian), and θ is the angle of diffraction (radian).

The dislocation density (δ) is calculated by following formula, Eq. (3):

$$\delta = 1/D_\mathrm{p}^2 \quad (\mathrm{lines\,m^{-2}}). \tag{3}$$

Williamson-Hall equation, Eq. (4):

$$B\cos\theta = k\lambda/D + 4\varepsilon\sin\theta, \tag{4}$$

where B is FWHM of a diffraction peak (radian), $k = 0.94$ (for cubic structures), λ is the wavelength of X-ray used ($\lambda = 0.15406$ nm) (Cu-Kα radiation), D is crystallite size, and ε is lattice strain.

Particle sizes found as a result of XRD analy-

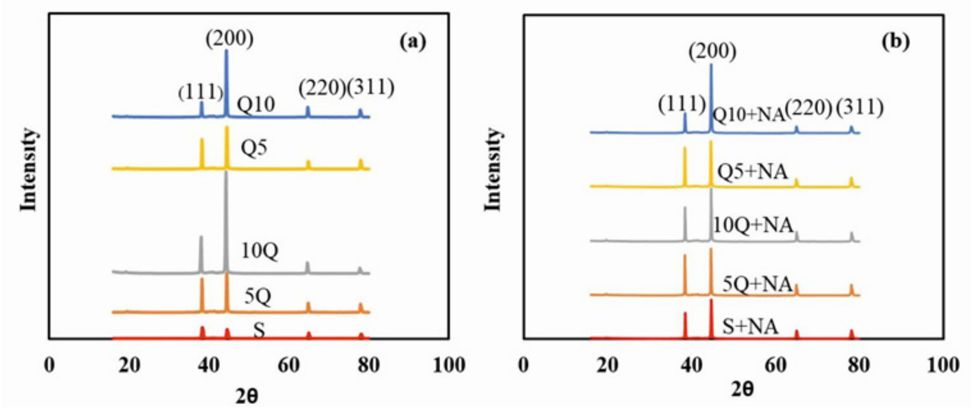

Fig. 7. XRD patterns of specimens (a) pre-deformed during RRA and (b) pre-deformed and naturally aged during RRA.

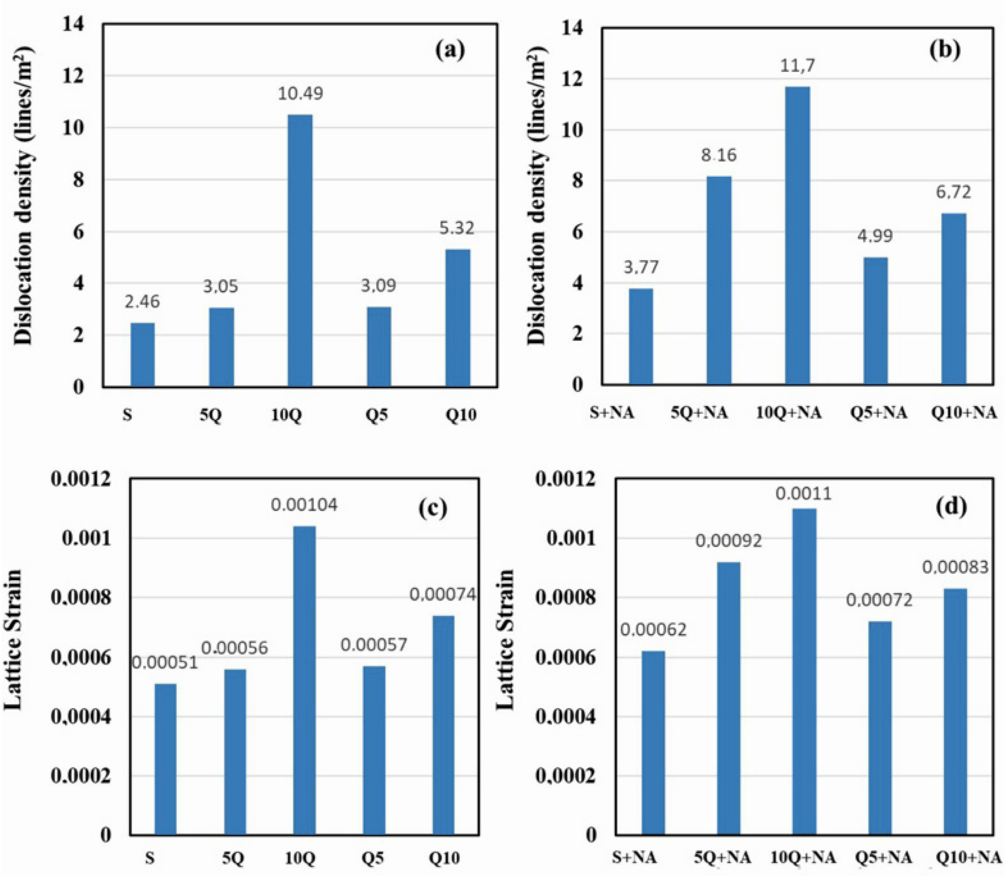

Fig. 8. Dislocation densities and lattice strain values of the specimens (a), (c) pre-deformed during RRA and (b), (d) pre-deformed and naturally aged during RRA.

sis are as follows: 5Q + NA is 350.11×10^{-10} m, Q5 + NA is 447.49×10^{-10} m, 10Q + NA is 292.18×10^{-10} m, Q10 + NA is 385.76×10^{-10} m, 5Q is 571.43×10^{-10} m, Q5 is 568.29×10^{-10} m, 10Q is 308.75×10^{-10} m, and Q10 is 433.27×10^{-10} m. The particle size of the specimens in which the RRA + NA was applied decreased compared to the specimens in which the RRA was applied. Therefore, Fig. 8 shows that the dislocation densities of the RRA + NA specimens also increased.

Texture always affects a polycrystalline material [35]. For polycrystalline materials, the texture coefficient of the specimens was calculated by Harris analysis [36]:

$$P\,(\mathrm{hkl}) = \frac{I\,(\mathrm{hkl})}{I_0\,(\mathrm{hkl})}\left[\frac{1}{1/n\sum_{i=1}^{n}\frac{I\,(\mathrm{h}_i\mathrm{k}_i\mathrm{l}_i)}{I_0\,(\mathrm{h}_i\mathrm{k}_i\mathrm{l}_i)}}\right], \quad (5)$$

If $P(\mathrm{hkl}) > 1$, it has orientation on the crystallographic plane (hkl). The texture coefficient values of the four crystallographic planes of the heat-treated specimens (111), (200), (220), and (311) were given in Eq. (5), Table 2. All of the specimens are oriented in the (200) plane. Q10 + NA and Q10 specimens made the highest orientation in the (200) plane. However, the 10Q specimen did not show dominant orientation as it was oriented in both the (200) and (220) planes.

Table 2. Texture coefficient values of crystallographic planes of heat-treated specimens applied to Al 7075 alloy

	Texture coefficient P (hkl)			
	111	200	220	311
S	0.56	1.62	0.84	0.98
5Q	0.63	1.52	0.88	0.96
10Q	0.51	1.78	1.18	0.81
Q5	0.54	1.9	0.69	0.87
Q10	0.31	2.56	0.61	0.52
S + NA	0.55	1.82	0.79	0.82
5Q + NA	0.68	1.71	0.79	0.8
10Q + NA	0.58	1.96	0.91	0.71
Q5 + NA	0.72	1.85	0.64	0.78
Q10 + NA	0.33	2.6	0.52	0.53

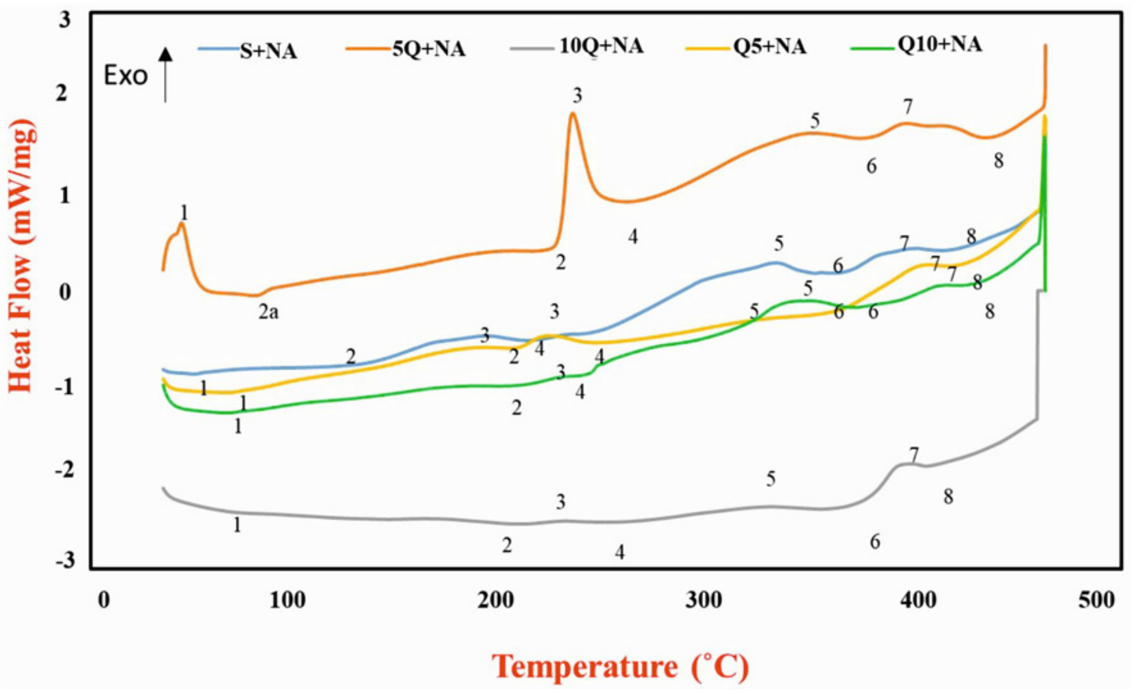

Fig. 9. DSC curves of Al 7075-T651 alloy, which was subjected to different pre-deformation and naturally aged during RRA.

3.4. DSC analysis

DSC analyses were performed to characterize the precipitates in the specimens and to see the phase transformations. Figure 9 shows the DSC curves of naturally aged specimens in which different pre-deformation was applied during the RRA heat treatment. It is seen that the DSC curve of the alloy Al 7075/T651 (S specimen) is similar to the other Al-Zn-Mg-Cu alloy specimens [37–40]. Aged Al alloys show a dissolution peak first, then a precipitation peak (possibly transition to equilibrium phase η'), and finally an endothermic peak corresponding to the dissolution of the remaining phases.

The first endothermic reaction results from the dissolution of the GP I regions. The first endothermic peak 1 in S + NA specimen occurred at 52 ℃. The second endothermic peak 2 at 131 ℃ resolved the GPII sites. It is seen that at 195 ℃, the exothermic peak 3 changed from GPII to η', and the η' phase dissolved at 215 ℃ (peak 4). When the temperature rises to 335 ℃ (peak 5), the η' phase changes to the η phase. At 350 ℃ (peak 6), the η phase dissolved. Finally, a final transformation took place at 390 ℃ (peak 7). The S-Al_2CuMg primary phase [41, 42] was dissolved at 425 ℃ (peak 8).

In 10Q + NA, Q5 + NA, and Q10 + NA specimens, the first endothermic peak (1) occurred at approximately 70 ℃. The peak temperature of the first reaction is similar for these three specimens. This indicates that the density of the GPI regions is also similar. It can also show that the sizes of the GPI regions are similar in the three specimens. Since all specimens have natural aging, the formation of GPI regions is significantly promoted. As seen in the microstructures, the precipitates of 10QR + NA, Q5R + NA, and Q10R + NA specimens are coarser. As the temperature increases, the dissolution of the coarser and more stable phase results from phase coarsening by the Ostwald ripening process [43]. In the 5Q + NA specimens, the GP I region dissolved at 45 ℃ (peak 1). This indicates that natural aging begins earlier than in other specimens. With a 5 % deformation effect in the 5Q + NA specimens, the GP II region (peak 2a) dissolved at 81 ℃. The GP II region re-dissolved at about 220 ℃ (peak 2). The reason for these two different dissolutions is thought to be related to the Zn/Mg ratios of the newly formed GP II zones. The GP II region changed sharply to the η' phase at 235 ℃ (peak 3), and the η' phase began to dissolve at 260 ℃ (peak 4). At 350 ℃ (peak 5), the η' phase changed to the η phase, and at 380 ℃ (peak 6), the η phase dissolved. At 397 ℃ (peak 7), the conversion takes longer than in the S + NA specimens, and the S phase begins to dissolve at 435 ℃. It can be understood from this that 5 % pre-deformation during retrogression increased the transformation temperatures.

In the 10Q + NA specimens, the conversion rates are more uncertain than in the 5Q + NA specimens. At 204 ℃ (peak 2), GPII dissolved. At 248 ℃ (peak 3), the GPII zone changed to the η' phase. At 255 ℃ (peak 4), the η' phase dissolved. At 340 ℃ (peak 5), the η' phase changed to the η phase. At 375 ℃ (peak 6), the η phase dissolved. At 395 ℃ (peak 7), the η phase changed to the S phase, and at 410 ℃ (peak 8), the S phase dissolved. The low peak intensity indicates that the S phase dissolves quickly. In the Q5 + NA specimens, the GP II zone dissolved at 205 ℃ (peak 2). At 223 ℃ (peak 3), the GP II zones changed to the η' phase. At 251 ℃ (peak 4), the η' phase dissolved, and at 362 ℃ (peak 5), the η' phase changed to the η phase. At 360 ℃ (peak 6), the η phase dissolved. At 407 ℃ (peak 7), the η phase turns into the S phase, and at peak 8, it is seen that the S phase begins to dissolve. In the Q10 + NA specimens, the GP II zones dissolved at 205 ℃ (peak 2). At 238 ℃ (peak 3), the GP II zones changed to the η' phase. At 243 ℃ (peak 4), the η' phase dissolved, and at 350 ℃ (peak 5), the η' phase changed to the η phase. At 370 ℃ (peak 6), the η phase dissolved. At 410 ℃ (peak 7), the η phase changed to the S phase. However, the low endothermic peak intensity after peak 7 indicates that the S phase dissolves rapidly during the transformation.

4. Conclusions

In this study, the changes in the process were investigated by applying a new heat treatment route to the Al 7075/T651 alloy. The microstructure, mechanical properties, and changes in crystallography of the heat-treated Al 7075/T651 alloy were analyzed and discussed, and the following results were obtained:

(1) The secondary phases elongated with 5 % pre-deformation and became spherical after natural aging.

(2) Specimens with applied 10 % pre-deformation have less precipitate distribution than specimens with applied 5 % pre-strain.

(3) With natural aging after RRA, the phase volume ratios of all specimens increased.

(4) All specimens were oriented in the (200) plane. Only the 10Q specimen was oriented in both the (200) and (220) planes.

(5) The hardness of all specimens increased with natural aging applied after RRA. The highest hardness was found in the Q10 + NA specimen.

(6) The increase in pre-deformation also increased the phase transformation temperatures.

(7) The highest dislocation density and lattice strain were calculated in the Q10 + NA specimen.

Acknowledgements

This study has been supported by the Scientific Research Project Program of Gazi University (under Project Number 07/2019-15). The authors are grateful to Gazi University for its financial support and the provision of laboratory facilities.

References

[1] X. Peng, Q. Guo, X. Liang, Y. Deng, Y. Gu, G. Xu, Z. Yin, Mechanical properties, corrosion behavior and microstructures of a non-isothermal ageing treated Al-Zn-Mg-Cu alloy, Mater. Sci. Eng. A 688 (2017) 146–154. https://doi.org/10.1016/j.msea.2017.01.086

[2] M. Ozer, S. I. Aydogan, H. Cinici, A. Ozer, Effects of sintering techniques and parameters on microstructure and mechanical properties of Al-15Si-2, 5Cu-0.5 Mg compacts and Al-15Si-2, 5Cu-0.5 Mg/B4C composites, Materials Today Communications 30 (2022) 103192. https://doi.org/10.1016/j.mtcomm.2022.103192

[3] A. Güral, O. Altuntaş, Improving the impact toughness properties of high carbon powder metallurgy steels with novel spherical cementite in the bainitic matrix (SCBM) microstructures, Materials Chemistry and Physics 259 (2021) 124203. https://doi.org/10.1016/j.matchemphys.2020.124203

[4] L. Wan, Y. Deng, L. Ye, Y. Zhang, The natural ageing effect on pre-ageing kinetics of Al-Zn-Mg alloy, J. Alloys Compd. 776 (2019) 469–474. https://doi.org/10.1016/j.jallcom.2018.10.338

[5] J. Zhao, Z. Liu, S. Bai, D. Zeng, J. Wang, Effects of natural aging on the formation and strengthening effect of G.P. zones in a retrogression and re-aged Al-Zn-Mg-Cu alloy, J. Alloys Compd. 829 (2020) 154469. https://doi.org/10.1016/j.jallcom.2020.154469

[6] S. Wang, J. Jiang, G. Fan, G. S. Frankel, L. Zhen, Effects of long-term natural aging on the altered surface layer on an Al-Zn-Mg-Cu alloy and on corrosion properties, Electrochim. Acta 266 (2018) 34–42. https://doi.org/10.1016/j.electacta.2018.02.001

[7] G. Waterloo, V. Hansen, J. Gjønnes, S. R. Skjervold, Effect of predeformation and preaging at room temperature in Al-Zn-Mg-(Cu-Zr) alloys, Mater. Sci. Eng. A 303 (2001) 226–233. https://doi.org/10.1016/S0921-5093(00)01883-9

[8] L. K. Berg, J. Gjønnes, V. Hansen, X. Z. Li, M. Knutson-Wedel, G. Waterloo, D. Schryvers, L. R. Wallenberg, GP-zones in Al-Zn-Mg alloys and their role in artificial aging, Acta Mater. 49 (2001) 3443–3451. https://doi.org/10.1016/S1359-6454(01)00251-8

[9] Z. Yang, J. Banhart, Natural and artificial ageing in aluminium alloys – the role of excess vacancies, Acta Materialia 215 (2021) 117014. https://doi.org/10.1016/j.actamat.2021.117014

[10] R. Ferragut, A. Somoza, A. Tolley, Microstructural evolution of 7012 alloy during the early stages of artificial ageing, Acta Mater. 47 (1999) 4355–4364. https://doi.org/10.1016/S1359-6454(99)00315-8

[11] G. Sha, A. Cerezo, Early-stage precipitation in Al-Zn-Mg-Cu alloy (7050), Acta Mater. 52 (2004) 4503–4516. https://doi.org/10.1016/j.actamat.2004.06.025

[12] G. Dlubek, R. Krause, O. Brümmer, F. Plazaola, Study of formation and reversion of Guinier-Preston zones in Al-4.5at.%Zn-$x$at.%Mg alloys by positrons, Journal of Materials Science 21 (1986) 853–858. https://doi.org/10.1007/BF01117364

[13] F. Chun, Z. Y. Liu, A. N. Ning, Y. B. Liu, S. M. Zeng, Retrogression and re-aging treatment of Al-9.99%Zn--1.72%Cu-2.5%Mg-0.13%Zr aluminum alloy, Trans. Nonferrous Metals Soc. China 16 (2006) 1163–1170. https://doi.org/10.1016/S1003-6326(06)60395-6

[14] J. K. Park, A. J. Ardell, Microstructures of the commercial 7075 Al alloy in the T651 and T7 tempers, Metallurgical Transactions A 14 (1983) 1957–1965. https://doi.org/10.1007/BF02662363

[15] C. Panseri, T. Federighi, Evidence for the interaction between Mg atoms and vacancies in Al-Zn10%--Mg0.1% alloy, Acta Metallurgica 11 (1963) 575–584. https://doi.org/10.1016/0001-6160(63)90091-9

[16] K. A Yasakau, J. Tedim, M. L. Zheludkevich, M. G. S. Ferreira, Smart self-healing coatings for corrosion protection of aluminium alloys. In: Handbook of smart coatings for materials protection, Woodhead Publishing (2014), pp. 224–274. https://doi.org/10.1533/9780857096883.2.224

[17] L. F. Mondolfo, Aluminum alloys: Structure and Properties. Elsevier, 2013. ISBN 1483144828

[18] B. Cina, Reducing the susceptibility of alloys, particularly aluminium alloys, to stress corrosion cracking. U.S. Patent No. 3,856,584.24, (1974).

[19] B. Cina, B. Ranish, Aluminum industrial product. Pittsburgh: American Society for Metals (1974).

[20] S. P. Ringer, K. Hono, Microstructural evolution and age hardening in aluminium alloys: Atom probe field-ion microscopy and transmission electron microscopy studies, Materials Characterization 44 (2000) 101–131. https://doi.org/10.1016/S1044-5803(99)00051-0

[21] M. Raghavan, Microanalysis of precipitate free zones (PFZ) in Al-Zn-Mg and Cu-Ni-Nb alloys, Metallurgical Transactions A 11 (1980) 993–999. https://doi.org/10.1007/BF02654713

[22] J. Z. Liu, J. H. Chen, D. W. Yuan, C. L. Wu, J. Zhu, Z. Y. Cheng, Fine precipitation scenarios of AlZnMg(Cu) alloys revealed by advanced atomic-resolution electron microscopy study, Part I: Structure determination of the precipitates in AlZnMg(Cu) alloys, Mater. Char. 99 (2015) 277–286. https://doi.org/10.1016/j.matchar.2014.11.028

[23] A. Kverneland, V. Hansen, R. Vincent, K. Gjønnes, J. Gjønnes, Structure analysis of embedded nano--sized particles by precession electron diffraction. η'-precipitate in an Al-Zn-Mg alloy as example, Ultramicroscopy 106 (2006) 492–502. https://doi.org/10.1016/j.ultramic.2006.01.009

[24] J. Liu, R. Hu, J. Zheng, Y. Zhang, Z. Ding, W. Liu, Y. Zhu, G. Sha, Formation of solute nanostructures in an Al-Zn-Mg alloy during long-term natural aging, J. Alloys Compd. 821 (2020) 153572. https://doi.org/10.1016/j.jallcom.2019.153572

[25] S. Liu, M. Zhang, Q. Li, Q. Zhu, H. Song, X. Wu, M. J. Couper, Effect of quenching rate on strengthening behavior of an Al-Zn-Mg-Cu alloy during natural ageing, Materials Science and Engineering A 793 (2020) 139900. https://doi.org/10.1016/j.msea.2020.139900

[26] G. Sha, A. Cerezo, Early-stage precipitation in Al-Zn--Mg-Cu alloy (7050), Acta Materialia 52 (2004) 4503–4516. https://doi.org/10.1016/j.actamat.2004.06.025

[27] A. Khalfalla, A. Raho, S. Amzert, A. Djemli, Precipitation kinetics of GP zones, metastable η' phase and equilibrium η phase in Al-5.46wt.%Zn-1.67wt.%Mg alloy, Transactions of Nonferrous Metals Society of China 29 (2019) 233–241. https://doi.org/10.1016/S1003-6326(19)64932-0

[28] G. Altuntaş, O. Altuntaş, B. Bostan, Characterization of Al-7075/T651 alloy by RRA heat treatment and different pre-deformation effects, Transactions of the Indian Institute of Metals 74 (2021) 3025–3033. https://doi.org/10.1007/s12666-021-02369-5

[29] G. F Vander Voort, Metallography, Principles and Practice, Materials Park, ASM International (1999). ISBN: 978-0-87170-672-0

[30] A. Karaaslan, I. Kaya, H. Atapek, Effect of aging temperature and of retrogression treatment time on the microstructure and mechanical properties of alloy AA 7075, Metal Science and Heat Treatment 49 (2007) 443–447. https://doi.org/10.1007/s11041-007-0083-9

[31] Y. Lang, G. Zhou, L. Hou, J. Zhang, L. Zhuang, Significantly enhanced the ductility of the fine-grained Al-Zn-Mg-Cu alloy by strain-induced precipitation, Mater. Des. 88 (2015) 625–631. https://doi.org/10.1016/j.matdes.2015.09.023

[32] ASM, ASM Metals Handbook 10 Materials Characterization, (1998). ISBN: 9781627082112

[33] G. K. Williamson, W. H. Hall, X-ray line broadening from filed aluminium and wolfram, Acta Metallurgica 1 (1953) 22–31. https://doi.org/10.1016/0001-6160(53)90006-6

[34] P. Scherrer, Determination of the size and internal structure of colloid particles, Gottinger Nachr. Math. Phys. 2 (1918) 98–100. (in German) https://doi.org/10.1007/978-3-662-33915-2_7

[35] B. D. Cullity, Elements of X-ray Diffraction. Addison-Wesley Publishing (1956).

[36] G. B. X. Harris, Quantitative measurement of preferred orientation in rolled uranium bars, The London, Edinburgh, and Dublin Philosophical Magazine and Journal of Science 43 (1952) 113–123. https://doi.org/10.1080/14786440108520972

[37] J. Buha, R. N. Lumley, A. G. Crosky, Secondary ageing in an aluminium alloy 7050, Materials Science and Engineering A 492 (2008) 1–10. https://doi.org/10.1016/j.msea.2008.02.039

[38] F. Viana, A. M. P. Pinto, H. M. C. Santos, A. B. Lopes, Retrogression and re-ageing of 7075 aluminium alloy: Microstructural characterization, Journal of Materials Processing Technology 92 (1999) 54–59. https://doi.org/10.1016/S0924-0136(99)00219-8

[39] R. Ranganatha, V. A Kumar, V. S. Nandi, R. R. Bhat, K. Muralidhara, Multi-stage heat treatment of aluminum alloy AA7049, Transactions of Nonferrous Metals Society of China 23 (2013) 1570–1575. https://doi.org/10.1016/S1003-6326(13)62632-1

[40] S. Liu, C. Li, S. Han, Y. Deng, X. Zhang, Effect of natural ageing on quench-induced inhomogeneity of microstructure and hardness in high strength 7055 aluminum alloy, J. Alloys Compd. 625 (2015) 34–43. https://doi.org/10.1016/j.jallcom.2014.10.195

[41] D. Wang, Z. Y. Ma, Effect of pre-strain on microstructure and stress corrosion cracking of over-aged 7050 aluminum alloy, Journal of Alloys and Compounds 469 (2009) 445–450. https://doi.org/10.1016/j.jallcom.2008.01.137

[42] D. K. Xu, P. A. Rometsch, N. Birbilis, Improved solution treatment for an as-rolled Al-Zn-Mg-Cu alloy, Part II. Microstructure and mechanical properties, Materials Science and Engineering A 534 (2012) 244–252. https://doi.org/10.1016/j.msea.2011.11.073

[43] J. K. Park, A. J. Ardell, Correlation between microstructure and calorimetric behavior of aluminum alloy 7075 and Al-Zn-Mg alloys in various tempers, Materials Science and Engineering A 114 (1989) 197–203. https://doi.org/10.1016/0921-5093(89)90859-9